

Mars Express/Venus Express ASPERA-3/4 IMA solar wind moments

Robin Ramstad, Mats Holmström and Yoshifumi Futaana

January 26, 2017

The Analyser of Space Plasmas and Energetic Atoms (ASPERA-3/4) particles packages onboard Mars Express (MEX) and Venus Express (VEX) have performed measurements of the local plasma environments around Mars and Venus since January 2004 and April 2006, respectively. The orbits of both spacecraft regularly cross the planetary bow shocks (BS), allowing the Ion Mass Analyzer (IMA) instrument to sample the undisturbed solar wind distribution. We have developed a routine to reduce ASPERA-3/4 measurements in the solar wind to physical parameters (density n_{sw} , velocity v_{sw} , and temperature T_{sw}) which are compared to 1 AU monitors and MAVEN.

MEX/ASPERA-3 IN THE SOLAR WIND

The solar wind is nominally a cold, fast stream of light ions (mainly H^+ and He^{++} with minor contributions from heavy species) and electrons radiating radially from the Sun. As the solar wind encounters Mars, it induces currents in the planet's upper atmosphere, forming an induced magnetosphere that presents an obstacle to the solar wind (e.g. *Luhmann et al.* (2004)). Typically the solar wind is supersonic and forms a bow shock as it encounters the planet. Inside the shock boundary the solar wind distribution is mass-loaded, slowed and heated, significant influence from the planet on the solar wind can be expected to nominally extend only up to this point, although protons can be reflected at the bow shock into the otherwise undisturbed solar wind.

ASPERA-3 features the *Ion Mass Analyzer* (IMA) instrument, an ion mass-energy spectrometer mounted on the spacecraft main body (*Barabash et al.*, 2006), see Figure 1. The IMA ion optical assembly consists of a top-hat electrostatic energy analyzer (ESA) and a scanning electrostatic deflection system, achieving a solid angle elevation-azimuth coverage $\pm 45^\circ \times 360^\circ$.

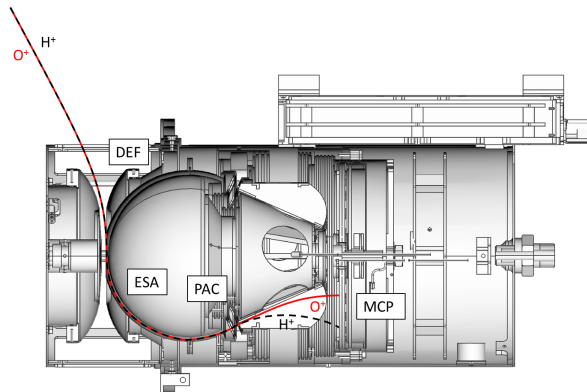


Figure 1: Hemicylindrical cut-away drawing of IMA with example ion trajectories overlaid. Two ions with the same energy and direction of movement are here guided by the deflection system (DEF) into the instrument and pass the electrostatic analyser (ESA), ensuring that all ions are roughly monoenergetic. The ions are subsequently accelerated by the post-acceleration (PAC) gap into the magnetic mass-separation chamber where ions with high masses are (in this example O^+) guided to the inner rings of the MCP and light ions are guided to the outer rings.

The ESA separates ions in the energy range 1 eV–32 keV with a resolution of $\frac{\Delta E}{E} = 7\%$. After passing the ESA, the ion beam is accelerated and focused by a post-acceleration (PAC) gap ion lens, increasing the beam energy by a setting of 300, 2433 or 4216 eV, referenced as PAC-0/4/7, respectively. Mass separation is achieved by magnetic separation of the nearly monoenergetic beam in a chamber with a toroidal magnetic field, dividing the beam by its constituent species' velocities (or mass/charge for a fixed energy) before these strike the microchannel plate (MCP). The MCP is divided into 16 azimuthal sector anodes and 32 mass-rings. Heavier ions (e.g. O^+) have larger gyroradii than light ions (e.g. H^+) and are directed to the inner mass rings while the lighter ions end up on the outer rings or strike the walls of the instrument. Every 192 seconds IMA is able to return a mass spectrum for 16

azimuths, 16 elevations and 96 energy levels, covering a $360^\circ \times 90^\circ$ field-of-view (FOV) for energy levels $E_i > 50$ eV. For $E_i < 50$ eV, the deflection voltage is always set to zero on ASPERA-3, resulting in an almost 2-dimensional $360^\circ \times 4.5^\circ$ FOV with 12 s full-spectrum cadence (Ramstad *et al.*, 2015).

The bow shock at Venus is stationary for most solar wind conditions (Zhang *et al.*, 2004) and results based on MEX crossings at Mars indicate, similarly, only a weak trend except for extremely low dynamic pressure (Hall *et al.*, 2016; Ramstad *et al.*, 2017). Thus we use the average solar wind bow shock model from Vignes *et al.* (2000) and impose an additional safety margin to exclude all but the most extreme ($\geq 95\%$) crossings. The Vignes *et al.* (2000) bow shock model is defined as a hyperbolic with parameters

$$L = 2.04, \quad \epsilon = 1.03, \quad x_0 = 0.64, \quad (1)$$

where L is the semi-latus rectum, ϵ is the eccentricity and x_0 is the location of the focus on the symmetry axis (x_{MSO}), all in units of Martian radii ($R_M = 3390$ km). An additional safety margin, dependent on distance from the x -axis, $R_{yz} = \sqrt{y^2 + z^2}$ is added as

$$x_{safe} = x_{BS} + (R_{yz}/4.5)^2 + 0.1. \quad (2)$$

A quick comparison with the crossings reported by Ramstad *et al.* (2017) is shown in Figure 2 showing 2.7% of crossings are outside the safety margin.

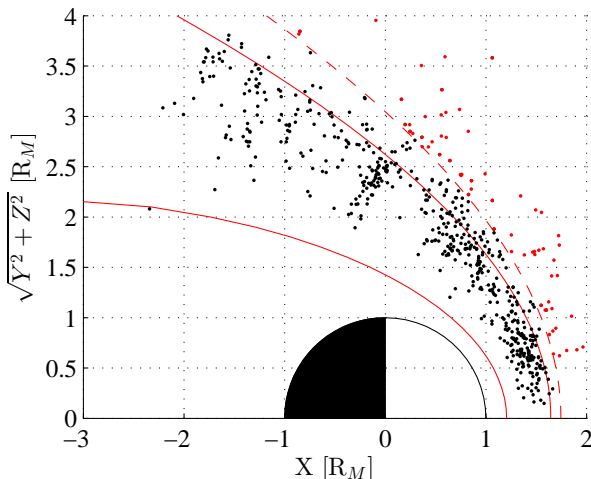


Figure 2: Mars bow shock crossings from Ramstad *et al.* (2017) (dots), nominal BS model from Vignes *et al.* (2000) (outer solid red line), with added safety margin (dashed red line) and magnetic pile-up boundary model (inner red line). Only crossings for $n_{sw} > 0.5 \text{ cm}^{-3}$ are included. Red dots are crossings outside the safety margin, representing 2.7 % of the total.

For every orbit, only IMA scans outside the safety margin are included. Next, it is assumed that the undisturbed solar wind is entering the instrument from the Sun-direction. Thus only FOV bins within $\pm 67.5^\circ$ azimuth and $\pm 13.5^\circ$ elevation are included in order to minimize noise and exclude reflected protons. This limited solar wind window is shown for an example scan in figure 3. The asymmetry of the box is due to internal scattering of protons $\lesssim 1$ keV inside the instrument that artificially spreads the signal to neighboring sectors. In a super-extreme scenario, where the solar wind angular distribution is extremely wide ($v_{sw} = 200$ km/s, $T_{sw} = 10^6$ K), this window catches roughly 80% of the corresponding Maxwellian distribution. Note that such conditions have never been observed for the duration of the mission.

From this point two individual data sets are constructed, one where each scan is treated individually (denoted SCAN-data) and another where the raw data from all valid scans in each orbit inbound/outbound segment is integrated (denoted ORB-data). Integrating the raw data increases the available counts for later processing (which is performed equally for both data sets), with the goal of producing reliable moments when count levels are low. Each dataset is collapsed over selected azimuths and elevations for each scan or scans, producing a mass-energy spectrum for each scan or orbit segment, respectively.

Occasionally the flux of solar energetic particles (SEPs) from the Sun is extremely high, particularly in connection with the arrival of coronal mass ejections (CMEs). The increased amount of penetrating radiation produces significant spurious counts across all MCP anodes independent of ESA voltages. The noise is cleaned under the assumption the IMA energy sweeps under 100 eV in the undisturbed solar wind represent dark-frame, i.e. signal free, measurements. The energy sweeps under 100 eV are combined to compute a mean noise profile for every mass-energy matrix which is subsequently subtracted from the raw matrix. An example result is shown in Figure 4 where the signal-noise level is reduced by almost three orders of magnitude. Additional noise-cleaning is performed by few-neighbor elimination, a coincidence scheme where counts below 10 is regarded as noise if there are less than two counts in either neighboring energy level (for the same mass-ring) or the neighboring mass-rings (for the same energy level).

At this stage the data preparation is completed, the data is analysed by separating the individual species by fitting Gaussian distribution functions. There are three populations to fit, two are for the protons and alphas that strike the MCP directly,

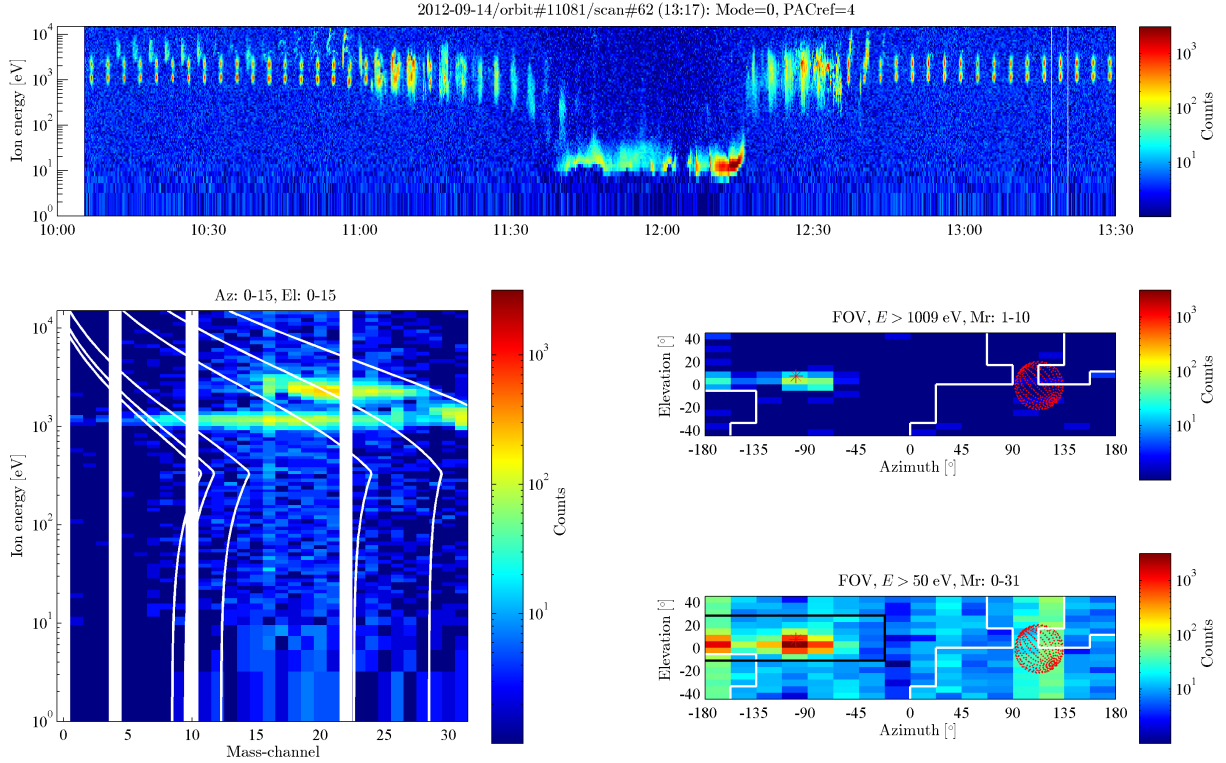


Figure 3: An example IMA scan, taken September 2012 in the solar wind. Top panel shows the full IMA time-energy spectrum for the orbit, integrated over all azimuthal angles and mass-rings, the white lines at 13:07 show the start and end times of the scan. Lower left panel shows the energy-mass spectrum for the scan with lines where ions with mass-per-charge (M/q) for major species are expected to strike the MCP. From left to right; CO_2^+ , O_2^+ , O^+ , He^+ , He^{2+} , H^+ . The lower right panels show the IMA FOV with space craft obstruction (white lines), planet grid (red dots) and the sun-direction (red star). The black box is centered around the Sun-direction and marks the FOV bins that are included in solar wind measurements. Note that sector 0 ($-180^\circ < \text{azimuth} < -157.5^\circ$) is influenced by cross-talk from other sectors and excluded. If the sun-direction is in a blocked direction the full scan is excluded.

centered at the positions of the respective mass-lines for each energy level. The third accounts for the protons below ~ 1.5 keV (for PAC-4) that strike the outer wall of the mass-separation chamber. A small fraction of these protons are reflected and scattered onto the MCP, producing a wide Gaussian centered over mass-ring #16. These so-called "ghost" protons are the only available proton signal below 1 keV and are accounted for. Figure 5 shows an example mass-energy matrix separated in its component protons, alphas and ghost protons. After mass-separation there is an energy-counts spectrum for each individual species. To reconstruct the original proton flux, different geometric factors are used for directly detected protons and proton ghosts. The conversion for protons is

$$F_{\text{H}^+,i} = \frac{1}{N_{\text{scans}}} \left(\frac{c_{\text{H}^+,i}}{G_{\text{H}^+,i}\tau/\Delta\Omega} + \frac{c_{\text{H}_{\text{gh}}^+,i}}{G_{\text{H}_{\text{gh}}^+,i}\tau/\Delta\Omega} \right), \quad (3)$$

where c_{H^+} and $c_{\text{H}_{\text{gh}}^+}$ are counts spectra for directly detected protons and proton ghosts, respectively. Similarly, G_{H^+} and $G_{\text{H}_{\text{gh}}^+}$ are the geometric factors for each species and τ is the integration time, set to 125 ms. The energy level E_i is indicated by the index i . The geometric factor is divided by $\Delta\Omega$, the space angle of an FOV bin, under the assumption that the entire solar wind angular distribution is covered by the IMA scan. The process of converting counts spectra to flux spectra is shown in Figure 6. Note that N_{scans} is included for ORB mass-matrices, which are produced by integrating measurements from several scans.

The flux spectra can be used to readily calculate density and velocity moments by integration:

$$n_{\text{H}^+} = \sum_i \frac{F_{\text{H}^+,i}}{\sqrt{2E_i/m_{\text{H}^+}}} \quad (4)$$

$$v_{\text{H}^+} = \frac{1}{n_{\text{H}^+}} \sum_i F_{\text{H}^+,i} \quad (5)$$

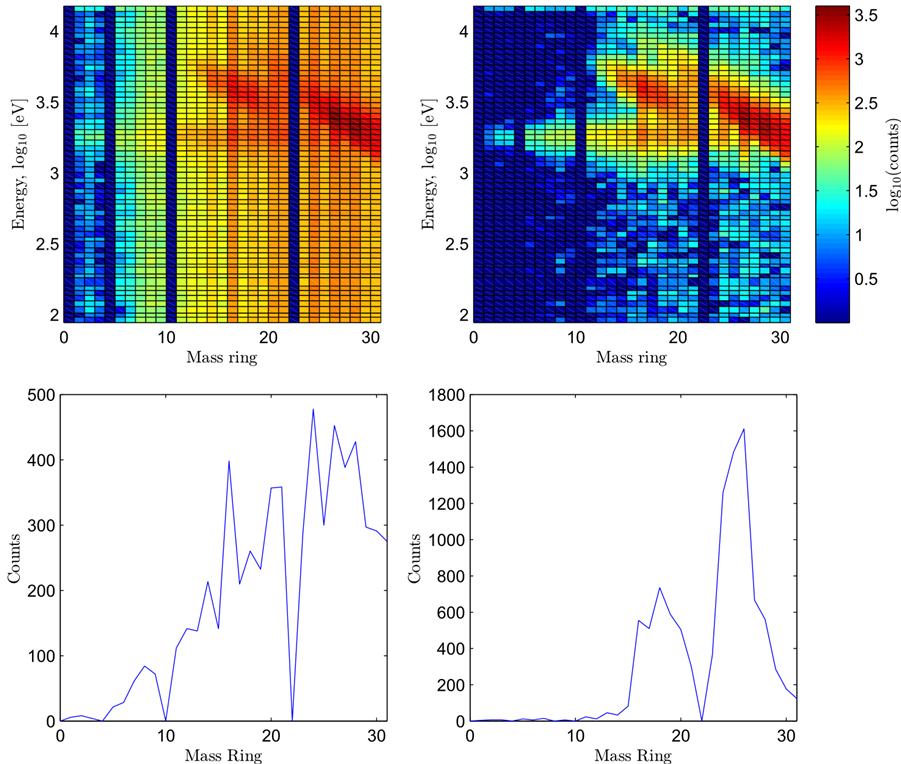


Figure 4: Example IMA scan in the solar wind on 2012-03-07 that has been heavily contaminated by strong SEP radiation (upper left), producing noise that rivals the signal intensity. The mean noise profile (lower left) over the mass-rings is subtracted from all energy steps, the resulting noise-reduced matrix is shown in the upper right panel. The count profile for the energy level 3.2 keV ($=3.5 \log_10$) is shown in the lower right panel.

The temperature moments T_{H^+} are highly susceptible to contamination if computed with integration. Instead these are calculated by fitting a Maxwellian function to the flux spectra. This fitting is also useful for assessing the quality of the moments, increased remnant noise or cross-species contamination will result in increased deviation from a Maxwellian shape, rendering worse goodness-of-fit. A "flag" parameter is calculated with the moments and set to 1 if $\sqrt{r}/\sum_i F_{H^+i} > 0.2$, where r is the residual norm. Additionally, flag=2 is set if the estimated temperature is below 2000 K, colder distributions can typically not be resolved by the common IMA energy tables at solar wind energies. Flag=3 is set if an uncalibrated PAC-setting was used by the instrument. If no issues are found then flag=0.

VEX/ASPERA-4 IN THE SOLAR WIND

A main point of this work is to develop IMA solar wind moments from MEX and VEX using the same algorithm, so as to make the resulting datasets easily comparable. However, a small number of differences exists between the instruments, space-

crafts and environments. To retrieve moments for all available solar wind measurements we have implemented an automatic shock detection routine based on ASPERA-4/ELS (electron spectrometer) and MAG (magnetometer) data, see Figure 7. For orbit-segments where the bow shock can not be confidently found we resort to using the average bow shock location and include a safety margin similar to the method for MEX. The Venusian bow shock model is different from the Martian model and described using the hyperbolic function from *Martinecz et al.* (2008),

$$L = 1.303, \epsilon = 1.056, x_0 = 0.788. \quad (6)$$

The safety margin is a function dependent on radial distance from the x -axis,

$$x_{\text{safe}} = x_{\text{BS}} + (R_{yz}/3.2)^2 + 0.25, \quad (7)$$

in units of Venusian radii, R_V .

After identifying which scans are in the solar wind, the measured distribution is integrated over all angles within $\pm 67.5^\circ$ azimuth and $\pm 13.5^\circ$ elevation from the Sun-vector (aberrated $\sim 5^\circ$), identical to the method for MEX. However, a large fraction of solar wind distributions appear significantly

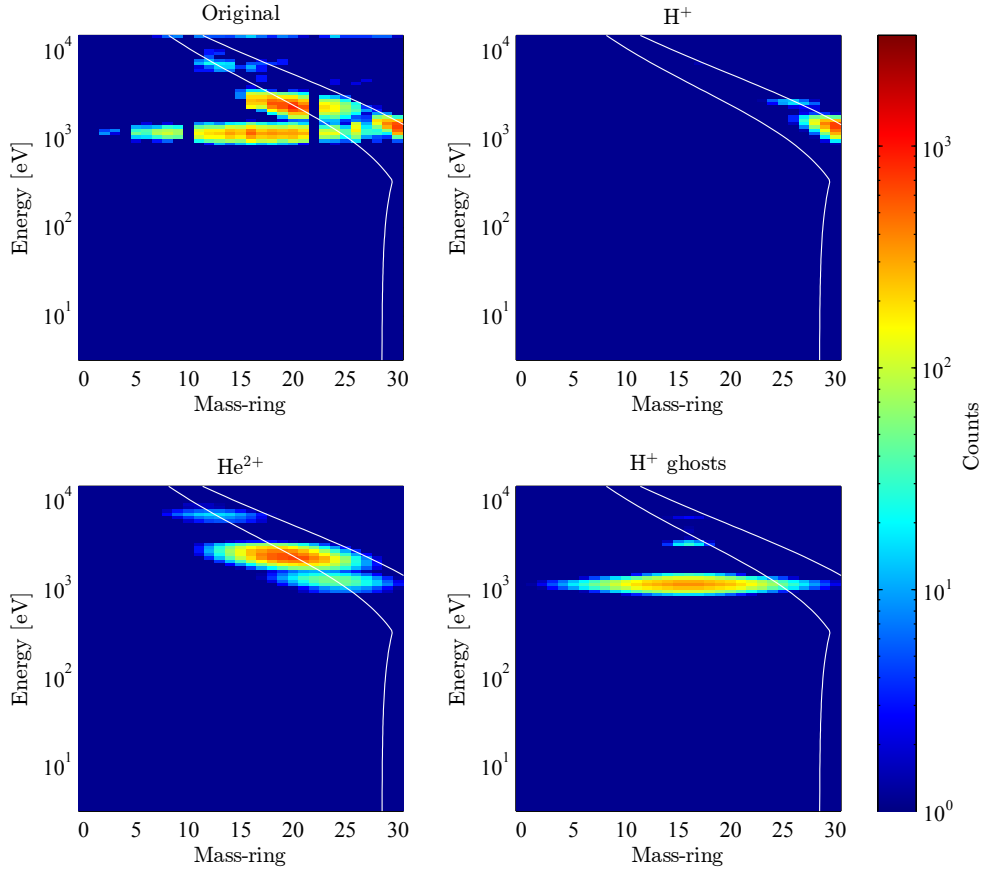


Figure 5: Example separation of ion species in an IMA ORB mass-energy matrix taken in the solar wind around 2012-02-23 05:00. Upper left panel shows the original matrix with noise-cleaned counts. Other panels are separated into ion species by fitting three Gaussian functions to the original counts for each energy level. Some cross-species contamination after fitting is always present but typically insignificant for protons. However alphas are strongly affected by proton ghosts for energy levels 2–3 keV where the centers of two distributions closely overlap.

deflected from the expected direction. Examples of such deflected distributions are shown in Figures 8 and 9. Deflected distributions are instead integrated around the angular bin with maximum counts and flagged in the final moments data set. The deflection angles are often larger than expected from aberration solely due to planet + spacecraft velocity.

Bulk noise is removed using presumed signal-free measurements under 100 eV similar to MEX. Remaining noise is cleaned using a 4D coincidence scheme where counts below the noise level without neighboring counts in either dimension are assumed to be outside a coherent distribution and set to zero.

Collapsing the distributions over angles yields a mass-energy matrix for each scan. Counts for each species are separated according to the expected striking location on the MCP by fitting multiple

Gaussian functions similar to for MEX, however the mass-lines are different and there is no proton ghost distribution. Instead ASPERA-4 IMA features significant cross-talk between mass-lines that needs to be subtracted (see Figure 9). The nature of this cross-talk is likely due to parasitic capacitance between individual anodes on the MCP (also manifesting as a widened distribution in azimuth). An example of a species-separated mass-energy matrix is shown in Figure 9.

The counts-energy spectra for each species can be converted to flux using the energy-dependent geometric factor, plotted in Figure 10. ORB moments for VEX are calculated simply as averages of the SCAN moments within 1/2 hour outside the BS as there is no need to improve the counts statistics in the manner required for MEX due to the low geometric factor for proton ghosts in ASPERA-3/IMA.

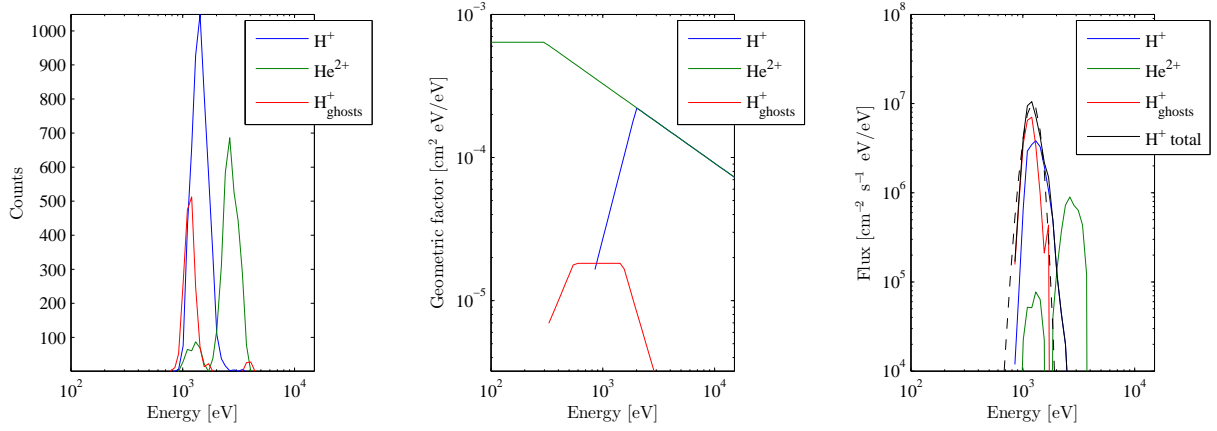


Figure 6: Progression of converting species-separated counts spectra (left panel) to flux (right panel) using the geometric factors (middle panel). The conversion for protons is performed as described by equation 3. This example ORB spectrum was produced from scans collected around 2015-01-02 23:00.

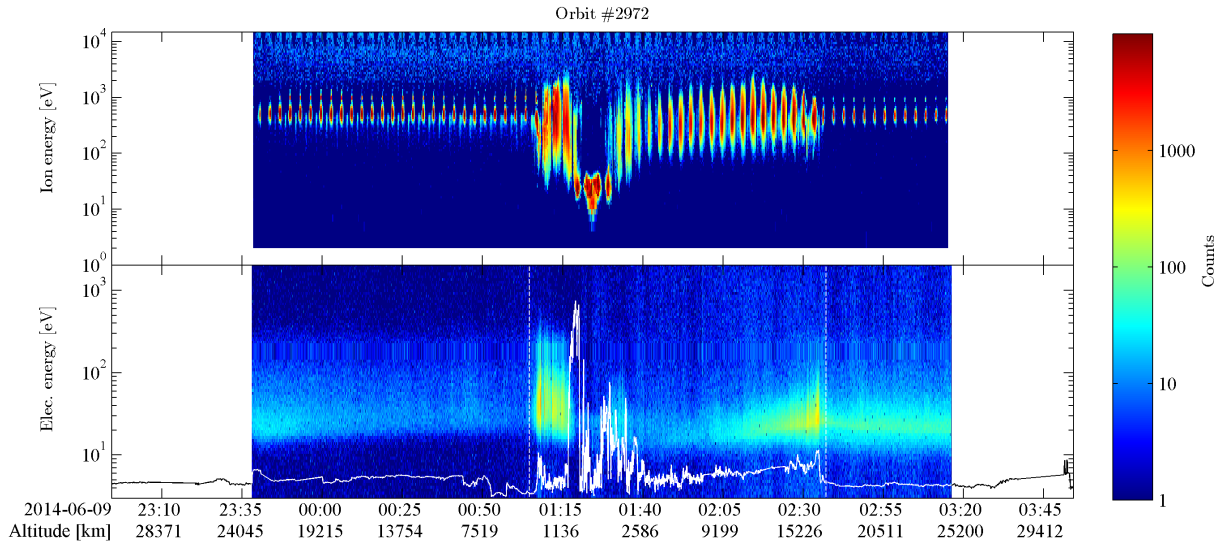


Figure 7: ASPERA-4 IMA data (upper panel), ELS data (lower panel) and normalized MAG data (solid white curve in lower panel) from 2014-06-09. The ELS and MAG data are used to automatically identify shock-like features which catch the bow shock and pre-shock disturbances. The crossings for this orbit are shown in the lower panel as vertical white dashed lines.

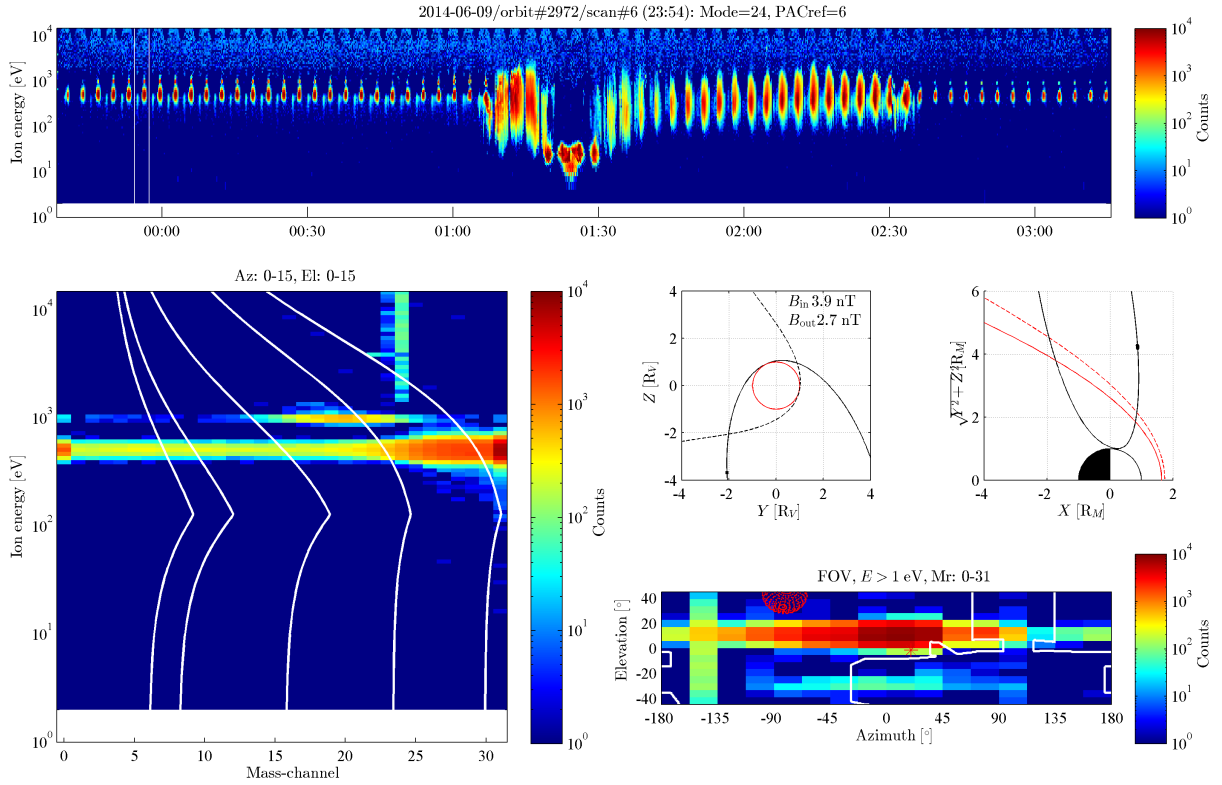


Figure 8: Example quickview plot of raw IMA data in the solar wind from 2014-06-09. The upper panel shows all time-series spectra integrated over all azimuthal sectors and mass-channels. The two vertical lines show the start/end times of scan #6. The energy-mass matrix from this scan is shown in the lower left panel. The middle-right panels show the orbit in VSO (solid lines) and estimated VSE (dashed lines) reference frames as well as cylindrical VSO with the average bow shock (red solid curve) and safety margin (dashed solid curve). The lower-right panel shows the IMA field of view (FOV) for this scan with the spacecraft shadowing displayed as white lines, the planet grid is as red dots and the Sun-direction is shown as a red star. The FOV plot shows that the solar wind is not entering the instrument from the expected direction but rather is deflected $\sim 10^\circ$, a feature that occurs when the Sun-direction is close to the spacecraft body.

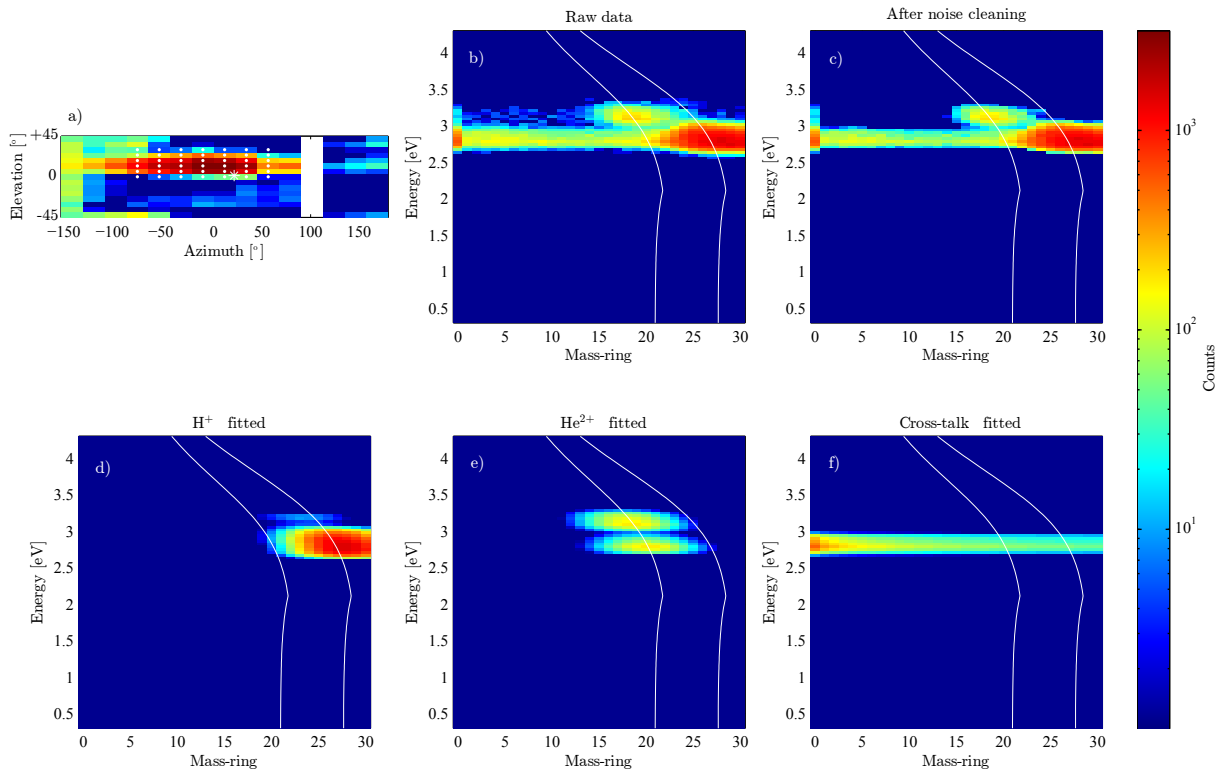


Figure 9: Example scan in the solar wind on 2014-06-09 00:42:00, processed to separate the counts for each species. a) angular distribution, showing a deflected distribution with dots marking included angular bins and white star marking the actual Sun-direction. b) Mass-energy matrix of raw counts collapsed over the marked angular bins in panel a), white lines mark expected location of H⁺ and He²⁺. c) Mass-energy matrix after noise cleaning. d) Fitted H⁺ counts. e) Fitted He²⁺ counts. f) Fitted cross-talk profile. Note that the cross-talk between species is insignificant for protons, but needs to be subtracted to compute alpha-fractions.

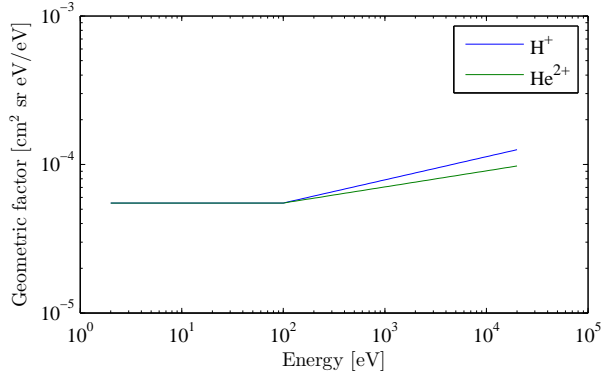


Figure 10: Venus Express ASPERA-4/IMA energy-dependent geometric factors for the main solar wind species.

The final VEX ASPERA-4/IMA moments are computed in the same manner as for MEX data (see equations 3 – 5), though without the proton ghost contribution which only exists in ASPERA-3/IMA.

RESULTS

The performance of the moments calculation can be checked by comparing with other solar wind monitors. Figures 13–18 show comparisons of the calculated IMA moments vs ACE/WIND (SWEPAM/SWIM) and STEREO-A/B (PLASTIC) moments that have been time-shifted (assuming a 27 d solar rotation period and measured drift-velocities) and intensity-scaled to Mars and Venus orbital positions. Times with CMEs, identified from a list by *Richardson et al.* (2013), have been treated differently accounting only for drift velocities. Comparisons of the average values of all IMA moments and ACE/WIND/STEREO-based moments are shown in Tables 1–2 for MEX and VEX, respectively. Reversely, the IMA average density scaled to 1 AU, assuming a time-averaged Mars-Sun distance 1.53 AU for Mars and 0.72 AU for Venus gives an equivalent density of 4.47 cm^{-3} for MEX and 4.35 cm^{-3} for VEX, indicating good agreement with the average density at Earth ($4\text{--}5 \text{ cm}^{-3}$).

	$n_{sw} [\text{cm}^{-3}]$	$v_{sw} [\text{km/s}]$	$T_{sw} [\text{K}]$
IMA	1.91	416	7.0×10^4
1 AU scaled	1.93	404	8.2×10^4

Table 1: Comparison of average Mars Express ASPERA-3/IMA solar wind moments and average ACE/WIND/STEREO moments from 2007-05-31 that have been scaled, in density, to Mars’ orbital position (1 AU scaled). Overall the agreement with 1 AU monitors is good.

	$n_{sw} [\text{cm}^{-3}]$	$v_{sw} [\text{km/s}]$	$T_{sw} [\text{K}]$
IMA	8.41	415	1.68×10^5
1 AU scaled	10.2	406	5.62×10^4

Table 2: Comparison of average Venus Express ASPERA-3/IMA solar wind moments and average ACE/WIND/STEREO moments from 2010-03-20 that have been scaled, in density, to Venus’ orbital position (1 AU scaled). Density and velocity agree well on average, however temperatures are significantly higher compared to the 1 AU monitors.

A 2D-distribution of the density, n_{sw} , and velocity, v_{sw} , of the MEX moments is shown in Figure 11. The fast solar wind and CME branches are readily visible along with extreme events. The equivalent distribution for VEX is shown in Figure 12, indicating a rather different

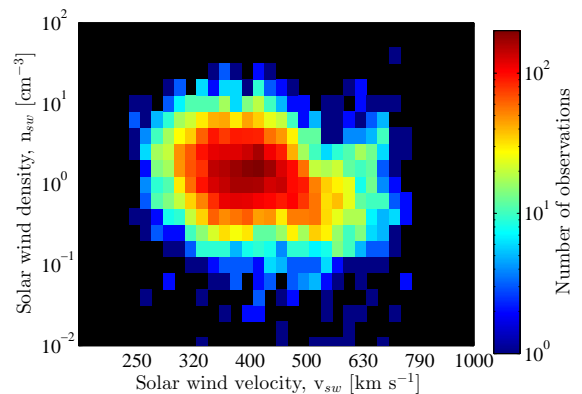


Figure 11: Logarithmic 2D-distribution of solar wind density, n_{sw} , and velocity, v_{sw} at Mars produced with the calculated IMA (ORB) moments. The data covers the time-period May 2007–February 2016. Black represents conditions that have not been observed.

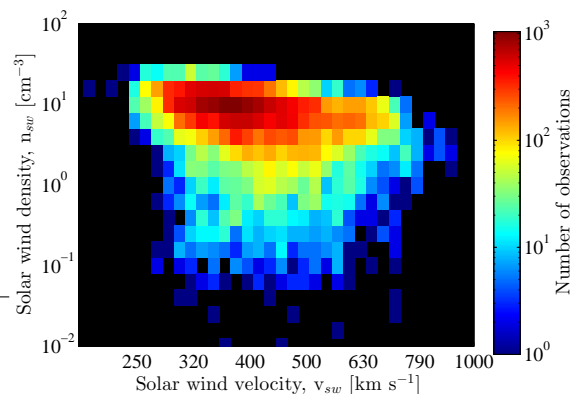


Figure 12: Logarithmic 2D-distribution of solar wind density, n_{sw} , and velocity, v_{sw} at Venus produced with the calculated IMA (SCAN) moments. The data covers the time-period March 2010–November 2014. Black represents conditions that have not been observed.

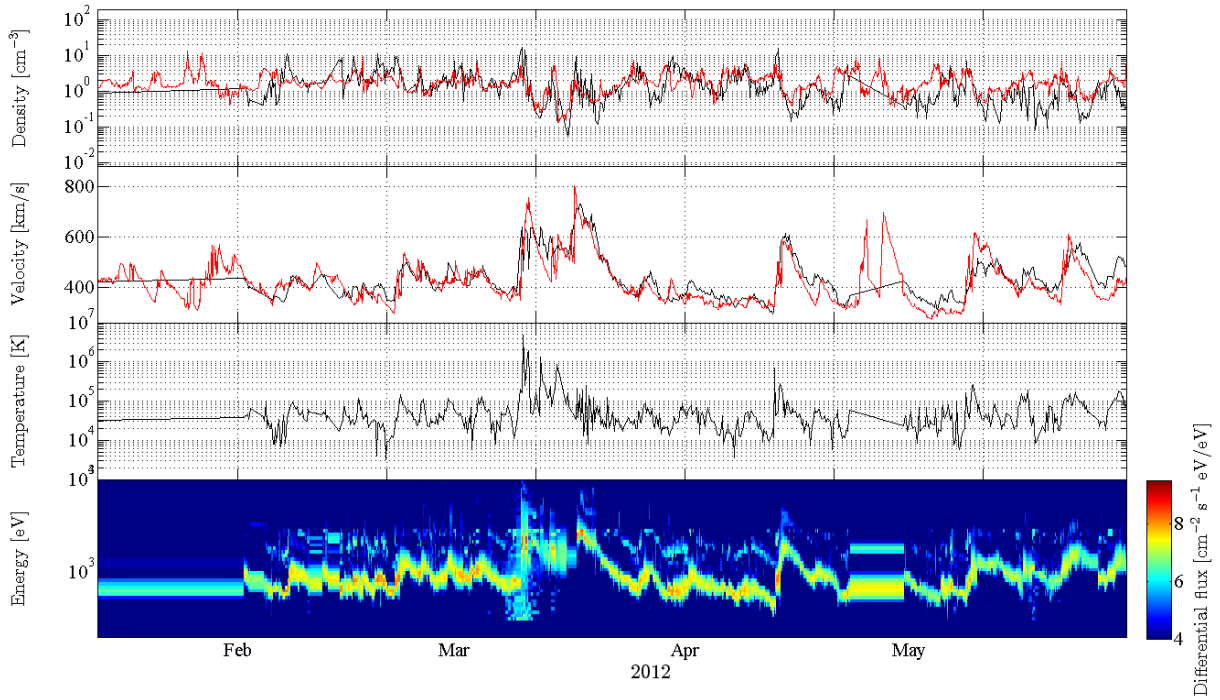


Figure 13: Comparison of calculated MEX ASPERA-3/IMA solar wind moments (black lines) and ACE/WIND moments (red lines) that have been time-shifted and intensity-scaled to Mars' position. Earth was in inferior conjunction to Mars in early March, the time surrounding shows the best agreement. The time-shifted moments do not include temperature, thus no such comparison can be made currently. The lowest panel shows the measured solar wind spectra used to calculate the moments, some remnant SEP noise can be seen on March 7.

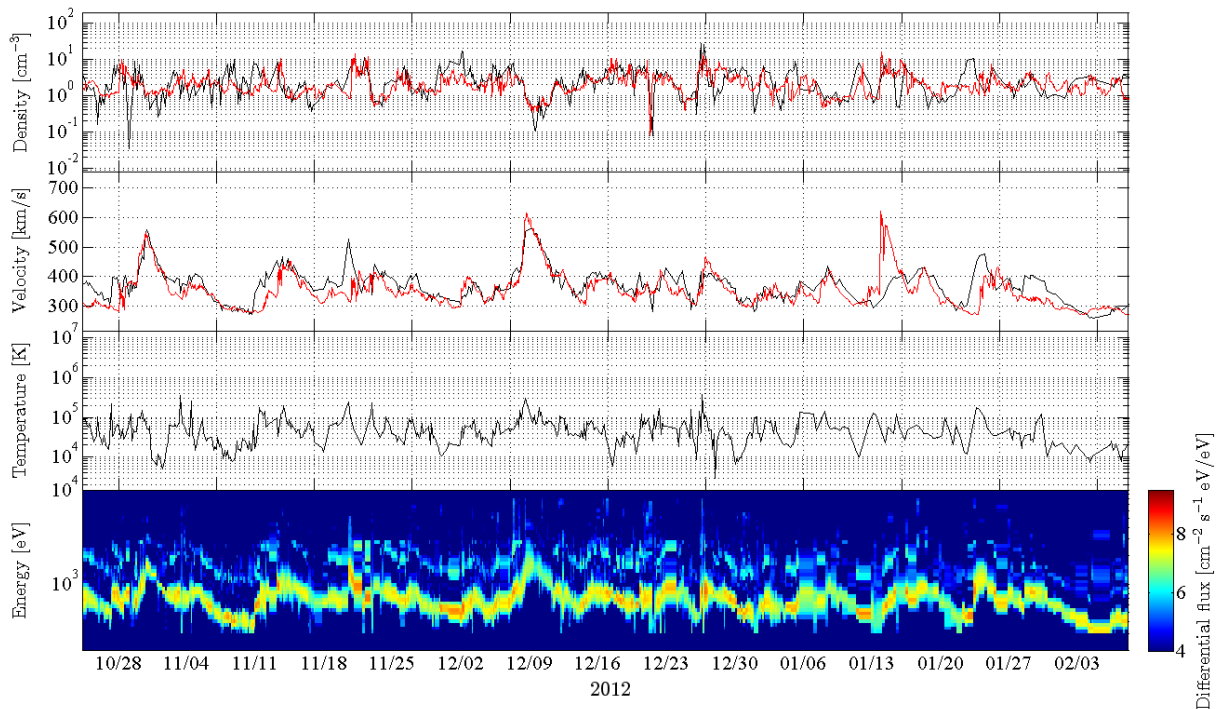


Figure 14: Comparison of calculated MEX ASPERA-3/IMA solar wind moments (black lines) and STEREO-B moments (red lines) that have been time-shifted and intensity-scaled to Mars' position. STEREO-B was in inferior conjunction to Mars in early December, the time surrounding shows the best agreement. The time-shifted moments do not include temperature, thus no such comparison can be made currently. The lowest panel shows the measured solar wind spectra used to calculate the moments.

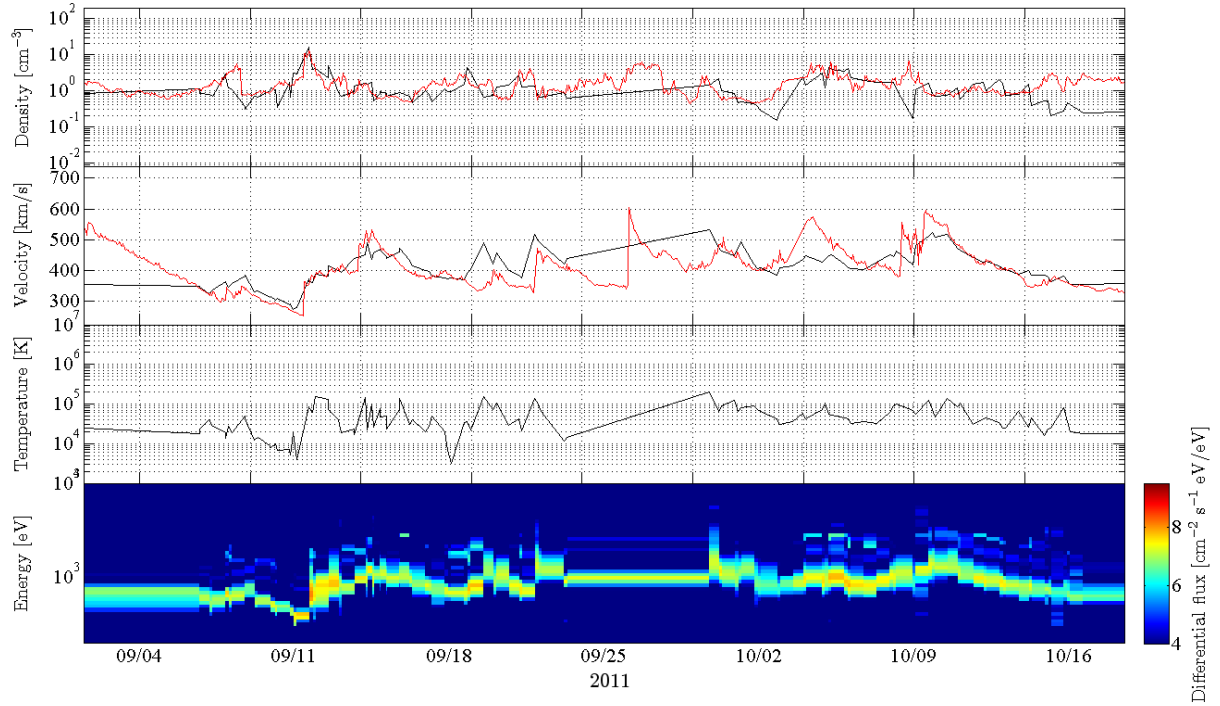


Figure 15: Comparison of calculated MEX ASPERA-3/IMA solar wind moments (black lines) and STEREO-A moments (red lines) that have been time-shifted and intensity-scaled to Mars' position. STEREO-A was in inferior conjunction to Mars in late August. The time-shifted moments do not include temperature, thus no such comparison can be made currently. The lowest panel shows the measured solar wind spectra used to calculate the moments.

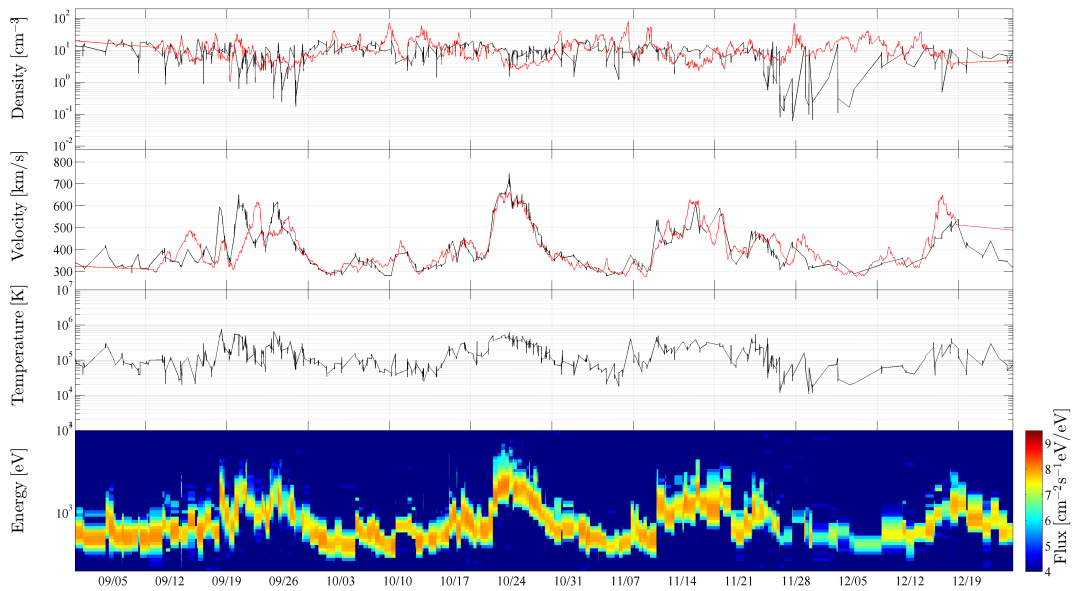


Figure 16: Comparison of VEX ASPERA-4/IMA SCAN moments and primarily ACE/WIND moments during Earth inferior conjunction in 2010. The time-shifted moments do not include temperature, thus no such comparison can be made currently. The lowest panel shows the measured solar wind spectra used to calculate the moments.

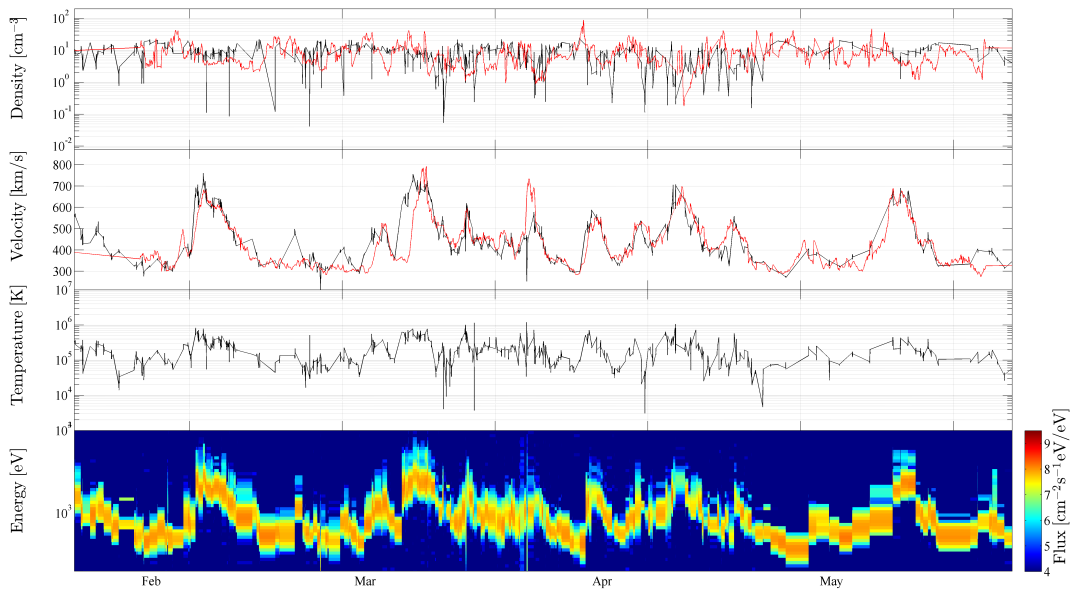


Figure 17: Comparison of VEX ASPERA-4/IMA SCAN moments and primarily STEREO-A moments during its inferior conjunction in 2011. The time-shifted moments do not include temperature, thus no such comparison can be made currently. The lowest panel shows the measured solar wind spectra used to calculate the moments.

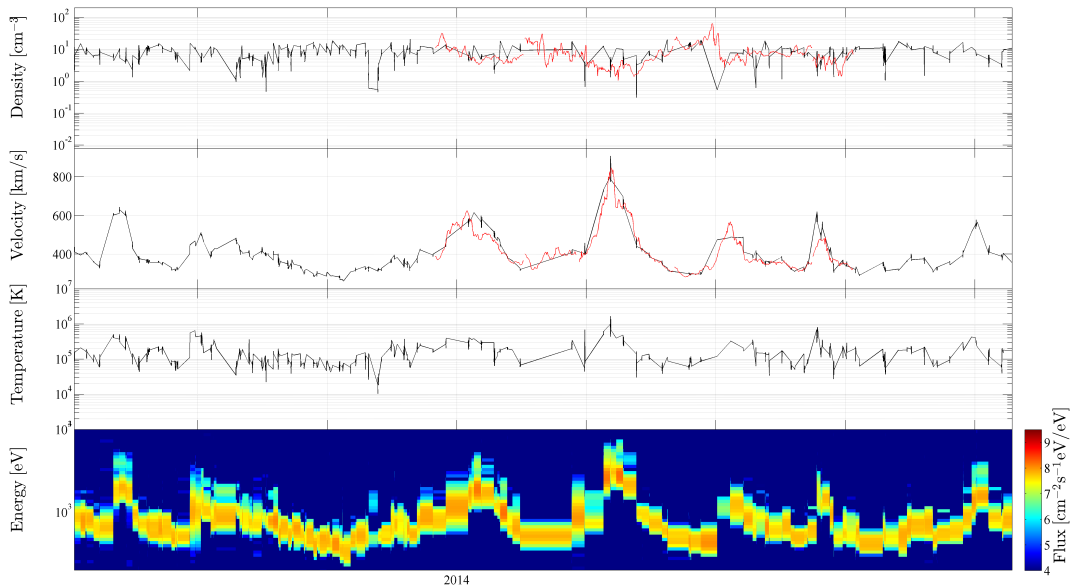


Figure 18: Comparison of VEX ASPERA-4/IMA SCAN moments and downstream ACE/WIND moments during Earth inferior conjunction in 2014. The time-shifted moments do not include temperature, thus no such comparison can be made currently. The lowest panel shows the measured solar wind spectra used to calculate the moments.

DISCUSSION AND CONCLUSIONS

Overall, the calculated MEX ASPERA-3/IMA moments appear to correlate well with expected parameters from upstream (1 AU) solar wind monitors at close conjunctions, indicating valid calibration.

A comparison with the Solar Wind Ion Analyzer (SWIA) instrument on NASA's MAVEN mission is shown in Figure 19. While velocities agree well, the fraction of the densities $f = n_{\text{SWIA}}/n_{\text{IMA}}$ is on average 1.9 with a median 1.58. The disagreement is strongest for low densities/high velocities, though at the current point it is unknown which instrument features the non-linear behavior.

The VEX ASPERA-4/IMA moments, computed analogously to the MEX moments, agree well with downstream monitors in terms of average density and velocity. However, the relative variations in density are smaller than expected from the comparison with 1 AU monitors and the average temperature is significantly higher than expected from a straight time-shifting. It is not known whether the deflected distributions frequently observed by IMA on VEX (see example in Fig. 9) are physical or an instrumental effect.

REFERENCES

- Barabash, S., et al. (2006), The Analyzer of Space Plasmas and Energetic Atoms (ASPERA-3) for the Mars Express Mission, *Space Sci. Rev.*, 126, 113–164, doi:10.1007/s11214-006-9124-8.
- Hall, B.E.S., et al. (2016), Annual variations in the Martian bow shock location as observed by the Mars Express mission, *J. Geophys. Res. Space Phys.*, 121, 113–164, doi:10.1002/2016JA023316.
- Luhmann, J.G., S.A. Ledvina, and C.T. Russell (2004), Induced magnetospheres, *Adv. Space Res.*, 33(11), 1905–1912, doi:10.1016/j.asr.2003.03.031.
- Martinez, C., et al. (2008), Location of the bow shock and ion composition boundaries at Venus – initial determinations from Venus Express ASPERA-4, *Planet. Space Sci.*, 56, 780–784, doi:10.1016/j.pss.2007.07.007.
- Ramstad, R., S. Barabash, Y. Futaana, H. Nilsson, X.-D. Wang and M. Holmström (2015), The Martian atmospheric ion escape rate dependence on solar wind and solar EUV conditions: 1. Seven years of Mars Express observations *J. Geophys. Res. Planets*, 120, doi:10.1002/2015JE004816.
- Ramstad, R., S. Barabash, Y. Futaana and M. Holmström (2017), Solar wind and EUV dependent models for the shapes of the Martian plasma boundaries based on Mars Express measurements *J. Geophys. Res. Space Phys., in revision*.
- Richardson, I. and H. Cane (2013), Near-Earth Interplanetary Coronal Mass Ejections Since January 1996, <http://www.srl.caltech.edu/ACE/ASC/DATA/level3/icmetable2.htm>, retrieved on 2013-05-29.
- Vignes, D., et al. (2000), The solar wind interaction with Mars: Locations and shapes of the Bow Shock and the Magnetic Pile-up Boundary from the observations of the MAG/ER experiment onboard Mars Global Surveyor, *Geophys. Res. Lett.*, 27(1), 49–52, doi:10.1029/1999GL010703.
- Zhang, T.L., K.K. Khurana, C.T. Russell, M.G. Kivelson, R. Nakamura, W. Baumjohann (2004), On the Venus bow shock compressibility, *Adv. Space Res.*, 33, 1920–1923, doi:10.1016/j.asr.2003.05.038.

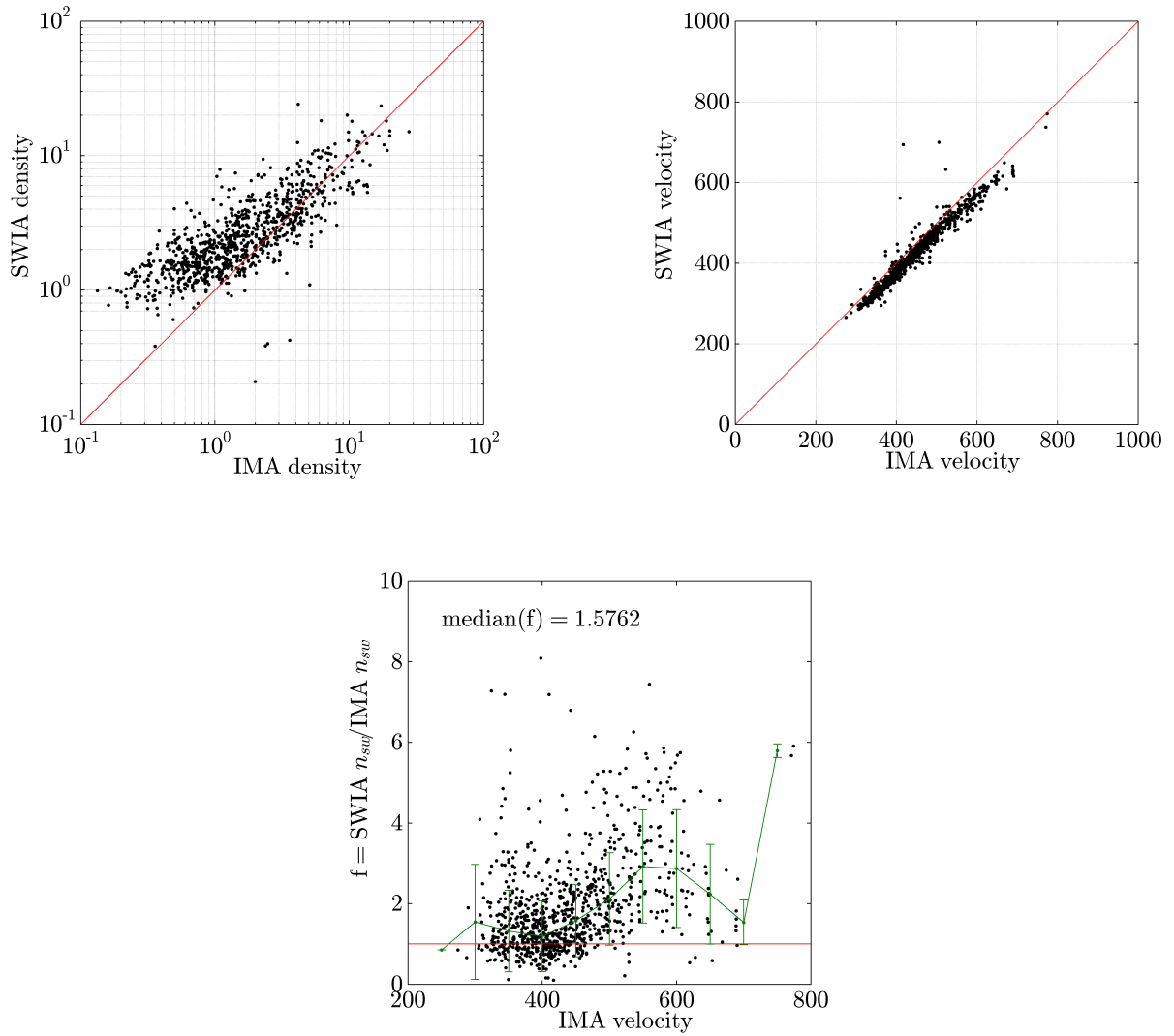


Figure 19: Comparison of calculated IMA ORB solar wind moments and MAVEN/SWIA orbit-averaged moments with separation between spacecraft constrained to less than 3 hours. Velocities agree well, though SWIA typically shows higher densities compared to IMA, particularly for low densities and high velocities. Units are in cm^{-3} and km/s for densities and velocities, respectively.